Int. J. Electrochem. Sci., 14 **(2019)** 9017 – 9029, doi: 10.20964/2019.09.74

International Journal of
ELECTROCHEMICAL
SCIENCE
www.electrochemsci.org

Copper Tungstate ($CuWO_4$) Nanoflakes Coupled with Cobalt Phosphate (Co-Pi) for Effective Photoelectrochemical Water Splitting

Chao Li[1,*], *Baiyu Guo*[1], *Ben Peng*[2], *Changsheng Yue*[2], *and Peng Diao*[1]

[1] Key Laboratory of Aerospace Materials and Performance (Ministry of Education), School of Materials Science and Engineering, Beihang University, Beijing 100191, China.
[2] Central Research Institute of Building and Construction Co. LTD., Energy Convention and Environment Protection Co. LTD., State Key Laboratory of Iron & Steel industry Environmental Protection, Beijing 100088, China.
[*]E-mail: nwpuvip@yeah.net

Received: 10 May 2019 / *Accepted:* 8 July 2019 / *Published:* 5 August 2019

Photoelectrochemical (PEC) water splitting provides us a green way to convert and utilize solar energy. In this work, Co-Pi was electrochemically deposited onto $CuWO_4$ nanoflakes (NFs) *via* a cyclic voltammetry (CV) method to enhance the photocatalytic performance of $CuWO_4$ toward PEC water splitting. The results demonstrated that the photocurrent density as well as the charge-transfer efficiency was improved within the entire potential range. Besides, the $CuWO_4$/Co-Pi exhibited an enhanced stability over the bare $CuWO_4$ in the phosphate buffer solution (pH 7) and an extremely high Faradaic efficiency (*ca.* 96%). Our work reveals that combination of $CuWO_4$ with Co-Pi is a feasible way to further enhance the performance of $CuWO_4$ photoanode toward PEC OER.

Keywords: Photoelectrochemical water splitting; copper tungstate; cobalt phosphate; electrochemical cocatalyst; oxygen evolution reaction

1. INTRODUCTION

PEC water splitting is an effective approach to resolving the challenge of increasing demand for sustainable energy. The overall water splitting consists of two key reactions: the oxygen evolution reaction (OER) and hydrogen evolution reaction (HER). The OER, a four-electron transfer process, is believed to be thermodynamically and kinetically more challenging as compared to the HER [1,2]. The two processes can be separately investigated *via* a PEC water splitting device [3]. In principle, n-type semiconductor, whose valence band edge lies in a more positive potential than the H_2O/O_2 oxidation potential (1.23 V *vs.* normal hydrogen electrode (NHE)), can be employed as the candidate photoanode

for PEC OER [4-9]. Copper tungstate ($CuWO_4$) is a typical n-type semiconductor with a bandgap value of *ca.* 2.3 eV [10-15], ensuring that solar light with a wavelength shorter than 540 nm can be absorbed. Besides, the valence band edge of $CuWO_4$ is located at *ca.* 2.60 V *vs.* NHE [16], therefore the holes generated in the valence band own enough driving force to oxidize water, thus making $CuWO_4$ a suitable candidate photoanode for PEC OER. Moreover, $CuWO_4$ exhibits other advantages such as environmentally friendly composition, high Faradaic efficiency [17], and outstanding stability within a wide pH range (pH≤9.5) during the chemical and photochemical course [10,12,17-20]. Over recent years, $CuWO_4$ has attracted increasing attention in PEC water splitting [9-27].

For large-scale application as a photoanode, the photoactivity of $CuWO_4$ toward PEC OER needs to be further enhanced. Accordingly, it is highly desirable to find out and then overcome the dominant limitations of $CuWO_4$ on the light-to-photocurrent conversion efficiency. Based on the previous find, there exists severe charge-carrier recombination at the $CuWO_4$/solution interface due to the slow kinetics of the OER as well as the intrinsic low surface properties caused by the mid-gap states regarding the localized Cu(3d) orbitals [16]. Modification of $CuWO_4$ with oxygen-evolving cocatalysts (OECs) is a feasible approach to addressing such issue since OECs exhibit superior capacity for efficiently capturing the photoinduced holes [28,29]. Noble metal oxides like RuO_2 [30] and IrO_2 [31] turn out as the most effective OECs toward OER. Whereas, the high cost inhibits their further implement in practical use. Among kinds of earth-abundant-composition and low-cost OECs including cobalt, iron, and nickel-based materials [32-34], Co-Pi has become the most widely-used OECs coupled with n-type semiconductor photoanodes such as ZnO [35,36], WO_3 [37], Fe_2O_3 [38-41], and $BiVO_4$ [42-44] to enhance the efficiency of the overall water splitting. Once modified with Co-Pi, the electron–hole recombination as well as the side reaction relative to the hole accumulation was partly suppressed, finally leading to an enhancement in OER performance.

Up to now, few reports have focused on the facilitation of charge-transfer course across the $CuWO_4$/solution interface. Davi *et al* combined $CuWO_4$ with a MnNCN-derived electrocatalyst, and a 12.5% increment of photocurrent density at 1.23 V *vs.* reversible hydrogen electrode (RHE) was achieved [45]. Lhermitte *et al* deposited manganese phosphate (Mn-Pi) onto the surface of $CuWO_4$, and the onset potential for the OER was negatively shifted by ∼100 mV [46]. Remarkable enhancement of the photocurrent density was achieved on Mn-Pi and Co-Pi modified $CuWO_4$/WO_3 composite photoanodes [47,48], which was 50% and 86% at 1.23 V *vs.* RHE, respectively. Whereas, the previous report suggested that maybe it was WO_3 that mainly contributed to the great increase in the photocurrent density [46]. Therefore, extensive efforts should be directed toward improving the charge-transfer efficiency at the $CuWO_4$/solution interface.

Herein, single-crystalline $CuWO_4$ NFs were synthesized *via* a sacrificial-template method and employed as the photoanodes for solar water oxidation. Co-Pi was electrochemically deposited onto $CuWO_4$ NFs *via* a CV method to accelerate the charge transfer process. The result demonstrated that the modification of $CuWO_4$ with Co-Pi not only increased the photocurrent density but also enhanced the charge-transfer efficiency within the entire potential range. Besides, the $CuWO_4$/Co-Pi photoanode exhibited a better stability in the phosphate buffer solution (pH 7) over the bare $CuWO_4$ and a high Faradaic efficiency (*ca.* 96%). Our work reveals that combination of $CuWO_4$ NFs with Co-Pi is an efficient way to further enhance the photocatalytic activity of $CuWO_4$ photoanode toward PEC OER.

2. EXPERIMENTAL

2.1. Chemicals and substrates

Tungsten powder, isopropanol (C_3H_8O), hydrogen peroxide (H_2O_2), 20wt% Pt/C, acetonitrile (C_2H_3N), urea (H_2NCONH_2), oxalic acid ($H_2C_2O_4$), hydrochloric acid (HCl), tungstic acid (H_2WO_4), acetic acid ($C_2H_4O_2$) were purchased from Beijing Chemical Works. Cupric nitrate trihydrate ($Cu(NO_3)_2 \cdot 3H_2O$), cobalt chloride hexahydrate ($CoCl_2 \cdot 6H_2O$) were purchased from Sinopharm Chemical Reagent Co., Ltd. All chemicals were analytically pure grade and used as received. Fluorine-doped tin oxide (FTO) substrates ($F:SnO_2$, 8 $\Omega \cdot sq^{-1}$, transparency 80%) were provided by Asahi Glass, Japan.

2.2. Preparation of WO_3 NF arrays

Tungsten powder (2 g) was dissolved in 10 mL of 30% hydrogen peroxide solution, and after the exothermic reaction ended, the resulting solution was diluted by adding 30 mL of isopropanol and 100 mL of deionized water to acquire the working electrolyte for the electrochemical deposition of WO_3 nanoseeds. The electrodeposition was conducted on a CHI 660E work station (CH Instruments Co.) with a conventional three-electrode cell, where a clean piece of FTO glass, a Pt mesh and a saturated calomel electrode (SCE) were used as the working, counter, and reference electrodes, respectively. The electrodeposition of WO_3 nanoseeds was carried out on the FTO glass *via* a two-step-potential deposition method, first at −0.40 V *vs.* SCE for 300 seconds and then 0.20 V *vs.* SCE for 15 seconds. After deposition, the nanoseeds-modified FTO substrates were sequentially washed with ethanol and water, then annealed in air at 450 ℃ for 30 minutes. The WO_3 NF films were obtained *via* a hydrothermal process. A mixture of 20 mg of urea, 20 mg of oxalic acid, 0.5 mL of 6 M HCl, 12.5 mL of acetonitrile, and 3.0 mL of 0.05 M H_2WO_4 was used to form the hydrothermal solution and then transferred to a 50 mL Teflon-lined stainless-steel autoclave. The WO_3-nanoseeds-modified FTO substrates were placed at an angle against the inside wall with the conductive sides facing down. The hydrothermal reaction was carried out at 180℃ for 2 hours, and the resulting WO_3 NFs were first rinsed with high-purity water and then blow-dried at room temperature in N_2 stream.

2.3. Synthesis of $CuWO_4$ NF arrays

$CuWO_4$ NF arrays were synthesized through a thermal solid-state reaction with the WO_3 NFs employed as sacrificial templates. In detail, $Cu(NO_3)_2 \cdot 3H_2O$ (0.725g) was dissolved in 30 mL acetic acid to obtain a 0.1 M solution. The resulting solution was drop cast onto the surfaces of the WO_3 NF templates (100 μL amount corresponds to an area of 3 cm × 1 cm) and being dried in air at room temperature. The drop-casting and drying procedures were repeated twice, and then the samples were subjected to a thermal treatment conducted in a muffle furnace at 550 ℃ for 1.5 hours. After annealing, a mixture of $CuWO_4$ and copper oxides was obtained. By immersing in 0.5 M HCl for 30 minutes to remove the copper oxides, the pure $CuWO_4$ NF arrays were finally acquired.

2.4. Electrodeposition of Co-Pi onto $CuWO_4$ NF arrays

The Co-Pi layer was deposited onto $CuWO_4$ NFs *via* a CV method. In detail, the deposition was conducted for required cycles within the potential range from -0.04 V to 1.15 V (*vs.* SCE) at a sweep rate of 50 mV s^{-1} in 0.1 M KH_2PO_4/K_2HPO_4 (KPi) buffer solution (pH 7) containing 0.5 mM $CoCl_2$. Note that the deposition solution was freshly prepared for each experiment.

2.5. Characterization

The crystal structures of the $CuWO_4$ and $CuWO_4$/Co-Pi photoanodes were characterized by X-ray diffraction (XRD) (Rigaku, rint2000 advance theta-2theta powder diffractometer) with Cu Kα radiation. The morphological characterization and energy dispersive X-ray spectra (EDS) were conducted on a Hitachi S-4800 field emission scanning electron microscope (FESEM) with an accelerating voltage of 5 kV. A Shimadzu 3600 UV–vis–NIR spectrophotometer was employed to collect the UV–vis diffuse reflection spectra. X-ray photoelectron spectroscopic (XPS) data were obtained on a Kratos AXIS Ultra DLD (Kratos Analytical Ltd, Japan) at a power of 150 W using Mg-monochromatic X-ray. All the binding energies were calibrated with the C 1s peak at 284.8 eV as the reference.

2.6. Electrochemical, photoelectrochemical, and oxygen detection measurements

All the electrochemical and PEC measurements were carried out on a CHI 660E work station (CH Instruments Co.) with a conventional three-electrode configuration, where the $CuWO_4$ or $CuWO_4$/Co-Pi photoanode, a Pt mesh and a saturated calomel electrode (SCE) served as the working, counter, and reference electrodes, respectively. In the linear sweep voltammetry (LSV), incident photon-to-current efficiency (IPCE), and electrochemical impedance spectroscopic (EIS) measurement, the photoanode was illuminated from the front side with an exposure area of 0.21 cm^2 and an incident light intensity of 100 $mW \cdot cm^{-2}$ provided by a 300 W xenon lamp. The data of IPCE were collected by measuring photocurrent densities at applied biases of 0.85 and 1.23 V *vs.* RHE under monochromatic light within the wavelength range from 350 to 600 nm. The detailed values were calculated using the following equation [49]:

$$IPCE = (1240J)/(\lambda I_{light}) \times 100\% \quad (1)$$

Where λ stands for the wavelength of the incident light (nm), J is the photocurrent density ($mA \cdot cm^{-2}$) obtained under the monochromatic light illumination with a certain wavelength, and I_{light} refers to the intensity of the incident light ($mW \cdot cm^{-2}$). Stability measurement was performed at 1.25 V *vs.* RHE with an area of 1 cm^2 exposed to illumination (150 $mW \cdot cm^{-2}$). The generated oxygen during the stability measurement was pumped into a sample loop every 30 minutes and further quantified *via* a gas chromatography (Shimadzu GC-2014c) equipped with a thermal conductivity detector (TCD). Before test, the PEC cell was purged with high-purity N_2 for 30 minutes to exclude the dissolved oxygen in the solution. All the electrochemical and PEC measurements were conducted in 0.1 M KPi buffer

solution (pH 7) with or without the addition of 0.1 M Na_2SO_3. All potentials in the work were measured against a SCE reference and converted to RHE potentials on the basis of the following equation [18]:

$$E_{RHE} = E_{SCE} + 0.0571*pH + 0.241 \quad (2)$$

3. RESULTS AND DISCUSSION

A typical SEM image of the $CuWO_4$ NFs is shown in Fig. 1a. The $CuWO_4$ sample presents a network structure composed of densely-grown and cross-intersected NFs perpendicular to the FTO substrate. This network structure with a large specific surface area favors not only the absorption of the incident light but also the transport of charge carriers, both leading to the superior photocatalytic activity toward PEC OER [18,19]. Fig. 1b shows the typical SEM image of the $CuWO_4$/Co-Pi sample. It can be seen that the network structure was maintained after Co-Pi deposition. While the surface of the sample became rougher, and the average thickness of the NFs became larger with the value increasing from *ca.* 65 nm to 75 nm (Fig. 1d and e show the detailed thickness distribution), indicating a thin layer of Co-Pi was deposited onto the $CuWO_4$ NFs. The result of EDS analysis displayed in Fig. 1c further demonstrates the presence of Co-Pi, as the signals of the element Co, P, Cu, W, and O are clearly identified in the EDS spectra. The crystal structures of the $CuWO_4$ NFs before and after Co-Pi modification were characterized by XRD measurement. As shown in Fig. 1f, the XRD patterns of the two samples well match that of the representative triclinic $CuWO_4$ phase (PDF 73-1823) [19]. All the data demonstrate that the deposition of Co-Pi does not cause an appreciable crystal structural change. Given the amorphous nature of Co-Pi [32], It is reasonable to understand that information about Co-Pi was hardly detected in the XRD measurement.

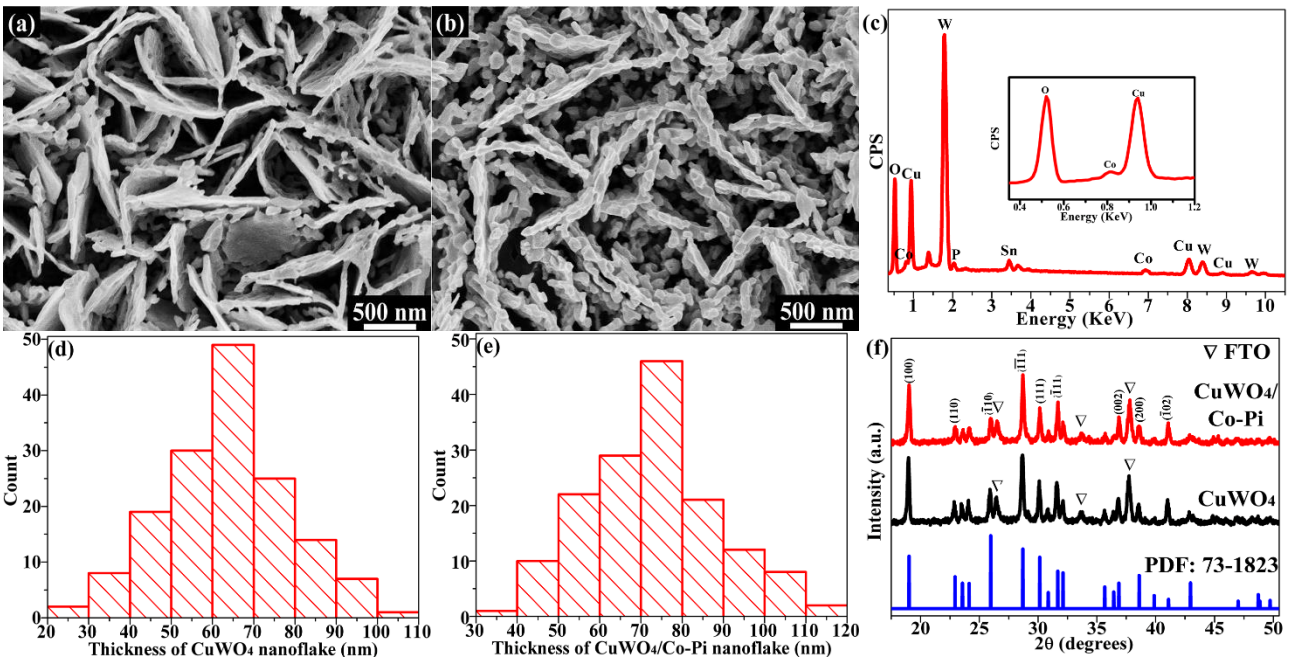

Figure 1. Typical SEM images of (a) $CuWO_4$ and (b) $CuWO_4$/Co-Pi. (c) EDS spectra of $CuWO_4$/Co-Pi; the inset shows the enlargement of EDS spectra in the range between 0.35 and 1.20 KeV (CPS, counts per second). The corresponding thickness distribution histograms of (d) $CuWO_4$ and (e) $CuWO_4$/Co-Pi (f) XRD patterns of $CuWO_4$ and $CuWO_4$/Co-Pi.

XPS measurement was conducted to gain insights into the detailed elemental composition and binding state for the $CuWO_4$/Co-Pi sample. The obtained survey scan and corresponding high-resolution spectra of Co 2p, P 2p are displayed in Fig. 2a, b, and c, respectively. The $CuWO_4$/Co-Pi sample is mainly composed of Cu, W, O, Co, P elements in addition to residual C, and the specific atomic ratio of Co to P is 23.36%:11.07%, nearly 2:1, consistent with the previous finding [32]. The relatively low contents of Cu (11.31%) and W (11.58%) detected here are primarily due to the limited penetration depth (~7 nm) of XPS measurement [42], suggesting that the elemental signals mainly came from the Co-Pi layer (~5 nm) wrapped around $CuWO_4$. For the high-resolution spectrum of Co 2p, two characteristic peaks presented at *ca.* 781 and 797 eV are attributed to Co^{2+} and Co^{3+} binding to oxygen, respectively [32,35,42]. While the typical peak at *ca.* 133.1 eV of P 2p spectrum corresponds well to the phosphate [32,35,42].

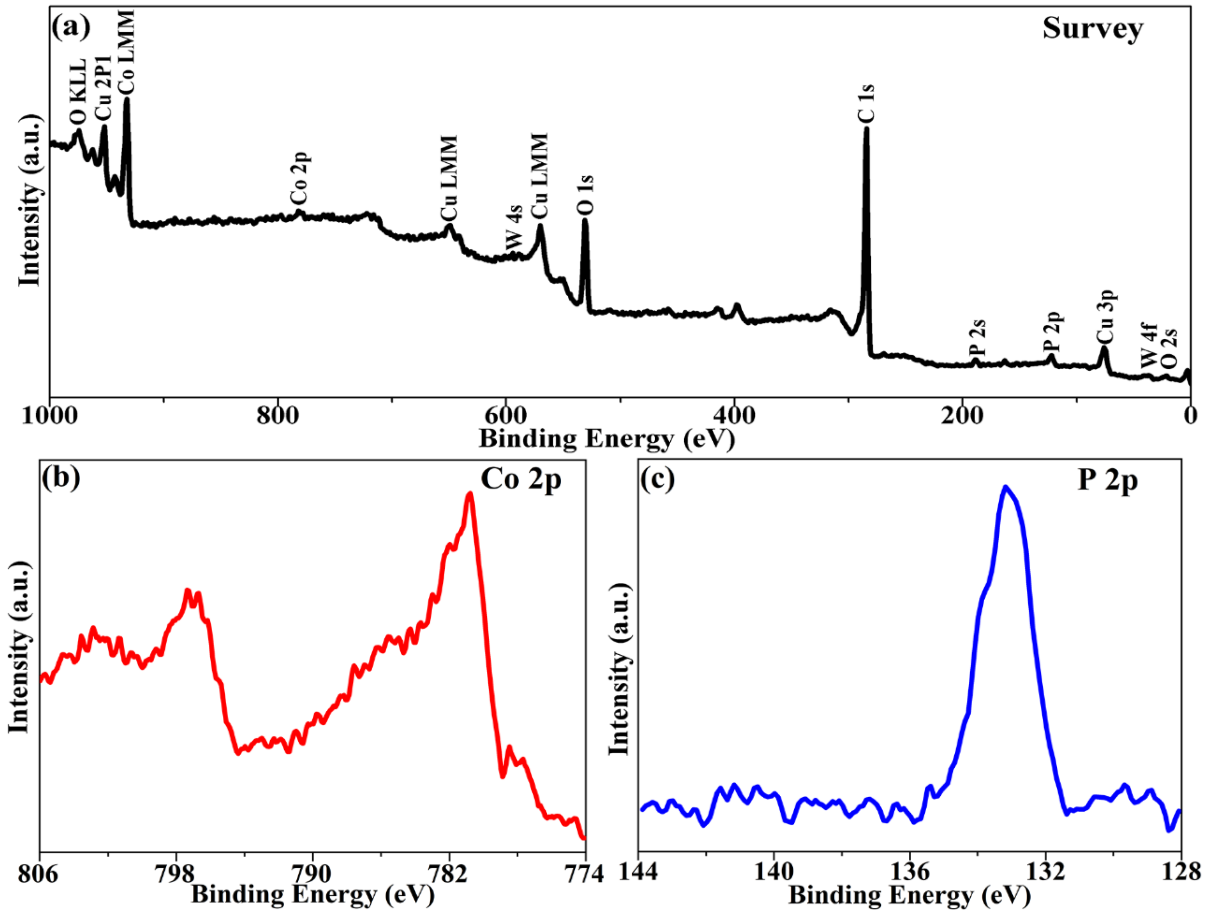

Figure 2. (a) XPS survey scan of the $CuWO_4$/Co-Pi sample; the corresponding high-resolution spectra of (b) Co 2p, and (c) P 2p.

CV measurements conducted on the $CuWO_4$ and $CuWO_4$/Co-Pi samples also provide the evidence for the successful deposition of Co-Pi, and the detailed results are shown in Fig. 3a. For comparison, CV curves obtained on the FTO and FTO/Co-Pi samples are displayed here as well. When coupled with Co-Pi, the CV curves of both the $CuWO_4$/Co-Pi and FTO/Co-Pi exhibit almost the same

oxidation and reduction characteristics. In detail, shoulder-like oxidation peaks due to the oxidation of Co^{2+} to Co^{3+} appear on both samples during the positive sweep [32,38,39], and much larger oxidation currents are observed as the potential becomes more positive, which arise from the catalytic oxidation of water to oxygen by Co-Pi [32,38,39]. During the negative sweep, broad cathodic peaks starting from 1.60 to 1.10 V *vs.* RHE are presented, and the peaks are correlated with the reduction of Co^{3+} back to Co^{2+} [32,38,39], considering the reduction of water to hydrogen is thermodynamically impossible within the potential window [50,51].

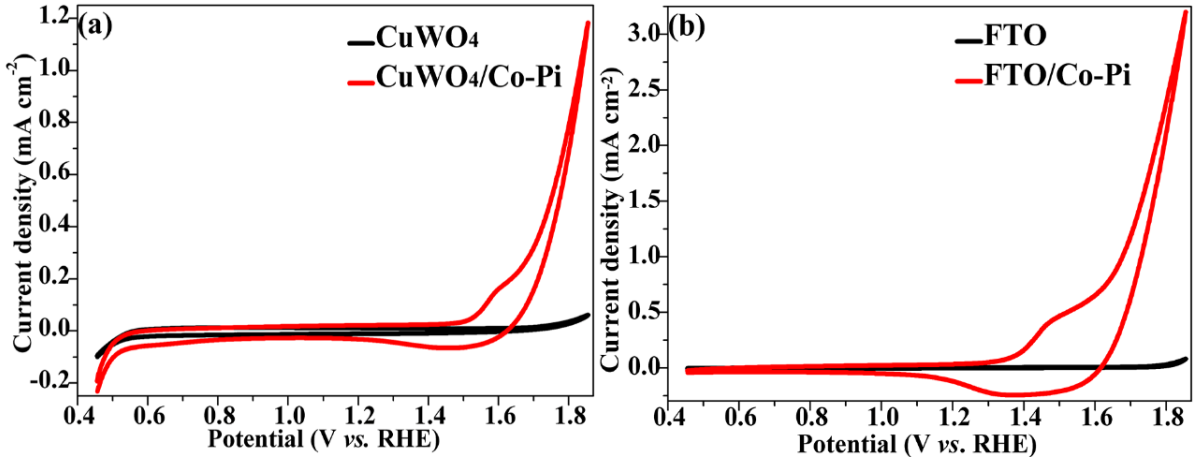

Figure 3. Cyclic voltammograms (CV) of (a) the $CuWO_4$ and $CuWO_4$/Co-Pi samples and (b) the FTO and FTO/Co-Pi samples at a potential sweep rate of 50 $mV \cdot s^{-1}$ under dark condition.

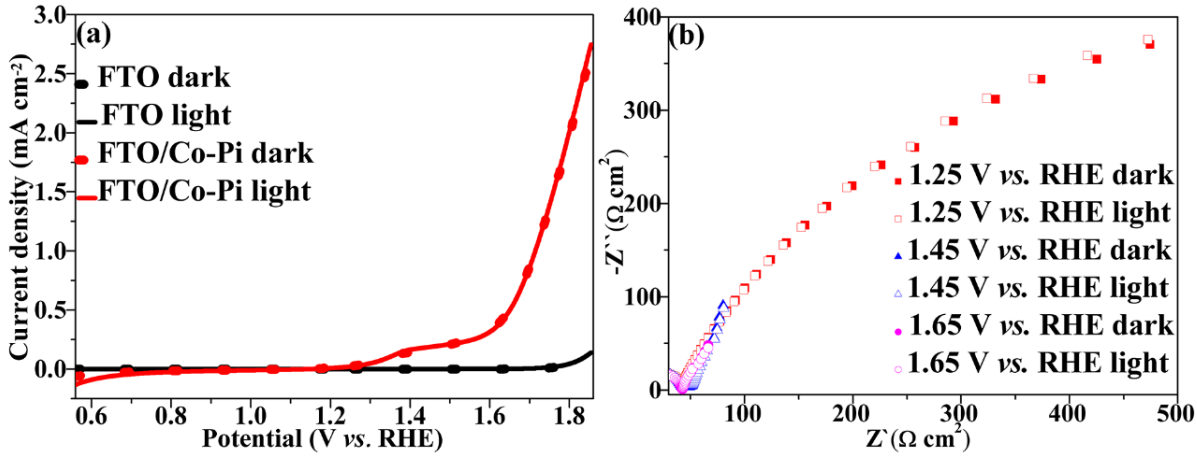

Figure 4. (a) *J-V* curves of the FTO and FTO/Co-Pi samples at a potential sweep rate of 10 $mV \cdot s^{-1}$ with or without illumination (100 $mW \cdot cm^{-2}$). (b) Nyquist plots of the FTO/Co-Pi sample at potentials of 1.25, 1.45, and1.65 V *vs.* RHE with or without illumination (100 $mW \cdot cm^{-2}$).

The photo-response behavior of Co-Pi was investigated by comparing the LSV curves recorded under dark and light conditions, and the results are shown in Fig. 4a. The current density versus potential (*J-V*) curves of Co-Pi with and without illumination nearly coincide with each other, revealing that Co-Pi does not show any photoactivity. The result is also supported by the EIS measurement. As shown in

Fig. 4b, the Nyquist plots obtained at 1.25, 1.45, and 1.65 V *vs.* RHE under dark and light conditions are almost identical to each other, meaning the reaction resistances keep constant before and after illumination. These results are quite different from those of a semiconductor, since the reaction resistance for a semiconductor would decrease dramatically when given the light due to the generation of photoinduced carriers. Note that all potentials chose here fulfill the requirement to trigger the OER.

Although Co-Pi does not show any photoactivity, it serves as an excellent cocatalyst for PEC OER when coupled with a photoanode. As previously reported, an improvement in the charge-transfer rate at the electrode/solution interface as well as an enhancement in the photoactivity toward PEC OER was achieved *via* Co-Pi modification [35-44]. Fig. 5a depicts the *J-V* curves of the $CuWO_4$ and $CuWO_4$/Co-Pi samples in 0.1 M KPi buffer solution (pH 7) under continuous illumination (100 $mW \cdot cm^{-2}$). Considering no obvious currents were generated on all the samples in the dark condition within the potential range from 0.65 to 1.25 V *vs.* RHE, we just displayed the photocurrent-potential curves here.

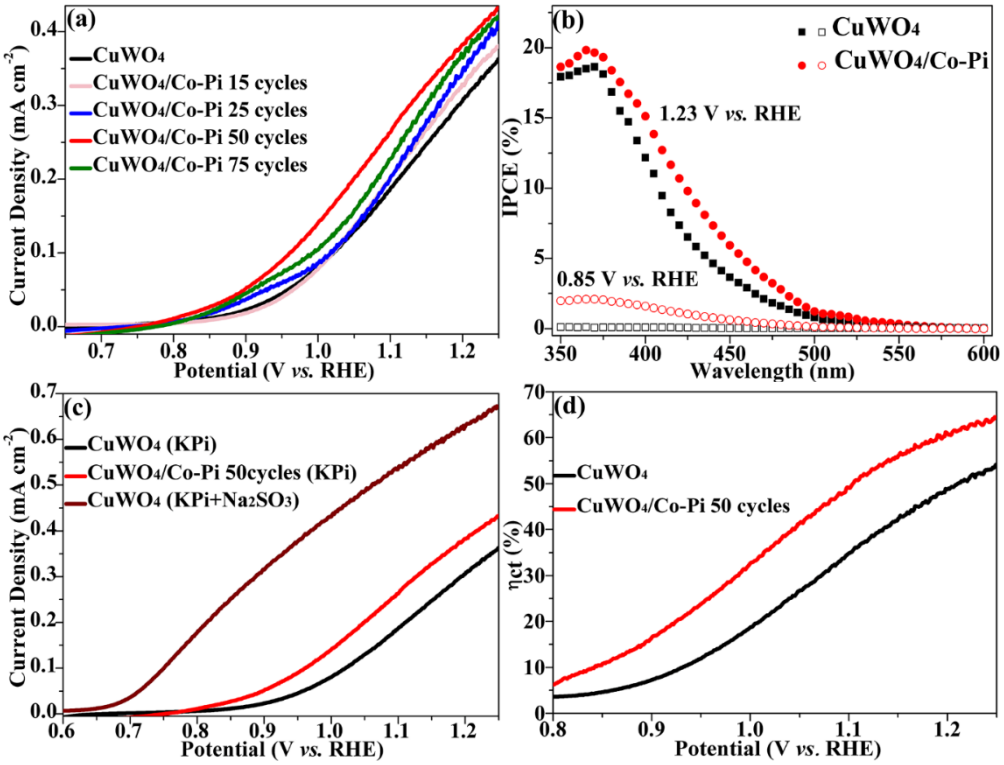

Figure 5. (a) *J-V* curves of the $CuWO_4$ and $CuWO_4$/Co-Pi samples with different deposition cycles under light condition (100 $mW \cdot cm^{-2}$). (b) IPCE values of the $CuWO_4$ and $CuWO_4$/Co-Pi (50 cycles) samples at applied potentials of 0.85 and 1.23 V *vs.* RHE. (c) *J-V* curves of the $CuWO_4$ and $CuWO_4$/Co-Pi (50 cycles) samples in contact with 0.1 M KPi buffer solution (pH 7) with or without 0.1 M Na_2SO_3 under dark and light conditions (100 $mW \cdot cm^{-2}$). (d) Interfacial charge-transfer efficiencies for the $CuWO_4$ and $CuWO_4$ /Co-Pi (50 cycles) samples at different working potentials.

As shown, all the Co-Pi-modified $CuWO_4$ samples exhibit improved photoactivities over the bare $CuWO_4$ toward PEC OER, with the $CuWO_4$/Co-Pi prepared under 50 deposition cycles revealing the maximum activity. In detailed, at 1.23 V *vs.* RHE, a 24% increase in the photocurrent density from 0.34 $mA \cdot cm^{-2}$ to 0.42 $mA \cdot cm^{-2}$ was achieved *via* Co-Pi modification. Herein, we believe the dependency

between the deposition cycle and photoactivity is due to the two opposite effects brought by the deposited Co-Pi layer. One is more active sites can be created with the increase of Co-Pi deposition cycle, which favors PEC OER; The other is the longer distance for the charge carrier to transport to the electrode/solution interface with Co-Pi layer being thicker, which is against PEC OER. Therefore, the highest activity of the $CuWO_4$/Co-Pi under 50 deposition cycles is the result of the balance between the two contrary effects.

The results of the IPCE measurements for both samples under applied potentials of 0.85 and 1.23 V *vs.* RHE are presented in Fig. 5b. The IPCE values of $CuWO_4$ at 0.85 V *vs.* RHE are almost 0% within the entire wavelength range, while an observable increment in the IPCE values at this potential was achieved after Co-Pi modification. These results agree well with the *J-V* curves displayed in Fig.5a, where no apparent photocurrent was generated on the bare $CuWO_4$ at 0.85 V *vs.* RHE, but appreciable photocurrent was perceived on the $CuWO_4$/Co-Pi sample. The similar enhancement effect was also achieved at 1.23 V *vs.* RHE with all the IPCE values of the $CuWO_4$/Co-Pi sample higher than those of the bare $CuWO_4$. These results undoubtedly demonstrate that an enhanced photoactivity for $CuWO_4$ toward PEC OER was achieved *via* Co-Pi modification.

In order to quantify the charge-transfer efficiency (η_{ct}) at the electrode/solution interface, PEC experiments in 0.1 M KPi buffer solution (pH 7) containing 0.1 M Na_2SO_3 were conducted. Na_2SO_3 is well known as an efficient hole scavenger with the capacity for rapidly consuming photogenerated holes to oxidize itself to Na_2SO_4, which results in the η_{ct} can be considered as approximately 100% in the presence of Na_2SO_3 [52,53]. Accordingly, the η_{ct} of a certain photoanode for PEC OER can be calculated using the following equation (3):

$$\eta_{ct} = J_{OER}/J_{Na2SO3} \quad (3)$$

Where the J_{OER} represents the value of the current density for PEC OER, and the J_{Na2SO3} stands for the corresponding value for oxidation of Na_2SO_3. Notable is that all the values are calculated by subtracting the dark current density from the total current density. As shown in Fig. 5c, much higher values of the photocurrent density were achieved in the presence of Na_2SO_3 due to the elimination of surface recombination. Besides, a more negative onset potential (*ca.* 0.60 V *vs.* RHE) for the OER was presented. Fig. 5d shows the variation of η_{ct} as a function of the applied potential, and from it we see that the η_{ct} value of the bare $CuWO_4$ exhibits a quite low value of *ca.* 4% near the onset potential region (0.80 V *vs.* RHE) and gradually increases with the applied potential being more positive. However, even at 1.25 V *vs.* RHE, the η_{ct} just reaches a value of *ca.* 52%, definitely revealing that a severe charge-carrier recombination exists at the $CuWO_4$/solution interface and consequently causes a serious photocurrent loss. After modification with Co-Pi, the η_{ct} values of the $CuWO_4$/Co-Pi were increased within the potential region from 0.80 to 1.25 V *vs.* RHE. For instance, the η_{ct} was shifted from *ca.* 52% to 65% at 1.25 V *vs.* RHE, suggesting that the surface recombination was partly suppressed by Co-Pi. All the data above definitely prove that adding Co-Pi improves the charge-transfer efficiency and thus leads to an enhanced PEC performance. Whereas, the photocurrent density obtained in the presence of Na_2SO_3 is much larger than that of the $CuWO_4$/Co-Pi, which shows that there still exists a huge room for the improvement in the photocurrent density.

Co-Pi is a widely-used OEC coupled with other common photoanode materials including ZnO [35], WO_3 [37], Fe_2O_3 [38-41], $BiVO_4$ [42,43]. As reported previously, when modified with Co-Pi, the

onset potentials for PEC OER could be even shifted close to the flat-band potentials [38]. Besides, the photocurrent densities at a certain potential could be improved by over 2 times [37,42,43]. While the enhancement effect achieved here for $CuWO_4$ photoanode is just moderate. These differences indicate that maybe the effect of a certain cocatalyst is dependent on the nature of the employed photoanode. Herein, we made a detailed comparison of the effect of Co-Pi OEC on $CuWO_4$ and other photoanodes, and the results are summarized in the Table. 1 below.

Table 1. Enhancement effects achieved on a photoanode *via* Co-Pi modification reported in the literatures

Ref.	Photoanode	J_{ph} (mA cm^{-2}) at potential (V *vs.* RHE)		Onset potential (V *vs.* RHE)	
		Before	After	Before	After
This work	$CuWO_4$	0.34 (1.23 V)	0.42 (1.23 V)	0.80	0.77
35	ZnO	0.02 (1.08 V)	0.03 (1.08 V)	0.48	0.25
37	WO_3	0.07 (0.81 V)	0.14 (0.81 V)	0.58	0.41
38	Fe_2O_3	0.30 (1.23 V)	0.50 (1.23 V)	1.00	0.65
40	Fe_2O_3	1.50 (1.23 V)	2.00 (1.23 V)	1.00	0.83
41	Fe_2O_3	1.40 (1.23 V)	2.20 (1.23 V)	1.00	0.88
42	$BiVO_4$	0.18 (1.16 V)	0.42 (1.16 V)	0.72	0.55
43	$BiVO_4$	0.60 (1.23 V)	1.60 (1.23 V)	0.72	0.70

J_{ph} represents the value of the photocurrent density obtained on a certain photoanode

Apart from the photocurrent density, long-term stability is also a crucial criterion to assess a photoanode material. Hence, chronoamperometric measurements for both photoanodes were carried out at an applied potential of 1.25 V *vs.* RHE with an exposure area of ~1 cm^2 under continuous illumination (150 mW·cm^{-2}). During the measurement, the amount of evolved oxygen was detected every 30 minutes *via* a gas chromatography. As shown in Fig. 6a, the $CuWO_4$ photoanode shows a moderate stability in 0.1 M KPi buffer solution (pH 7) with a decrease in the photocurrent density from the initial value (0.55 mA·cm^{-2}) to the final value (0.40 mA·cm^{-2}) after 4 hours' reaction. As for the $CuWO_4$/Co-Pi sample, only a slight decrease in the photocurrent density from 0.67 to 0.62 mA·cm^{-2} is observed, suggesting that an enhanced stability for $CuWO_4$ in KPi solution was achieved upon coupled with Co-Pi. A prominent stability means a steady enhancement in photoactivity *via* Co-Pi modification, which may probably be ascribed to the good adhesion between $CuWO_4$ and Co-Pi as well as the self-healing mechanism for Co-Pi in phosphate solution [54]. Fig. 6b shows the detailed results of the theoretical and actual amount of oxygen generated on both photoanodes, and the former value was calculated by assuming that all the photocurrents were produced from the OER. As shown, only a tiny deviation exists between the actual and theoretical value for the two photoanodes, suggesting that nearly all the photocurrents are contributed to the OER rather than some other side reactions. Faradaic efficiency can be derived from the value of the ratio between the actual and theoretical amount of O_2 [55], which is *ca.* 96% for both photoanodes. Exhibiting high Faradaic efficiency is definitely an outstanding merit for a

certain photoanode, especially when used to oxidize water to produce oxygen. Furthermore, the larger slope value of $CuWO_4$/Co-Pi than $CuWO_4$ also provides a strong authentication that modification with Co-Pi results in a better PEC performance, considering that the slope value can reflect the OER rate [55].

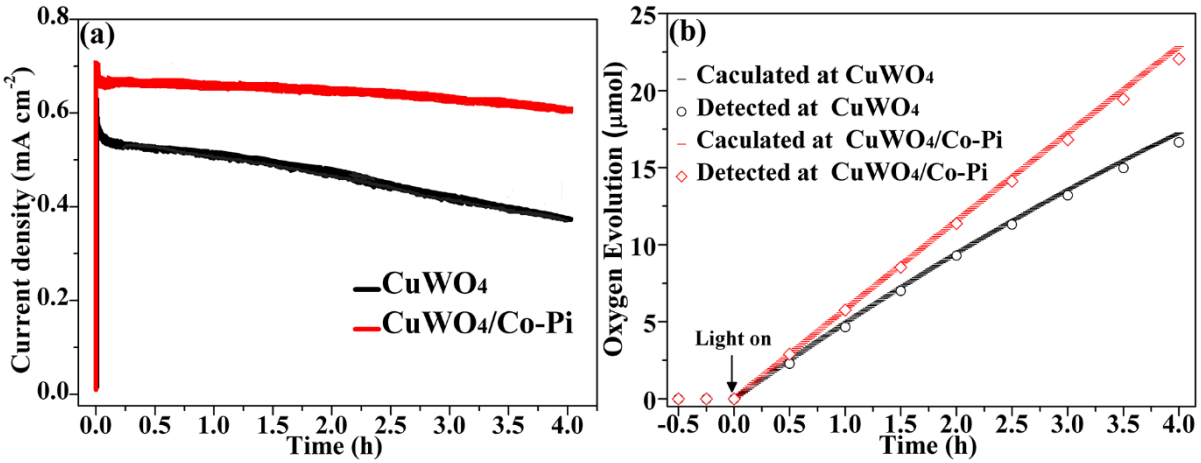

Figure 6. (a) Current density-time responses of the $CuWO_4$ and $CuWO_4$/Co-Pi (50 cycles) samples at the potential of 1.25 V *vs.* RHE under continuous illumination (150 $mW \cdot cm^{-2}$). (b) The detected and calculated amount of generated oxygen for the $CuWO_4$ and $CuWO_4$/Co-Pi samples.

Mechanism of the photoactivity enhancement *via* Co-Pi is illustrated in Fig. 7. When exposed to light, electron-hole pairs were generated in $CuWO_4$ photoanode. Due to the slow kinetics of water oxidation, the hole-transfer rate across $CuWO_4$/solution interface was limited. Meanwhile, the electron-hole pairs were continuously generated, therefore the recombination inevitably happened. Once Co-Pi was deposited onto the surface, it rapidly captured the photogenerated holes to oxidize Co^{2+} to its higher-valence-state ions like Co^{3+} and Co^{4+} with high activity to drive the OER [32,50,51], and accordingly reduced the propensity of surface charge recombination. Moreover, the Co^{3+} and Co^{4+} would be reduced back to the pristine Co^{2+} during the OER, ensuring a continuous enhancement in photoactivity *via* the oxidation-reduction cycle between Co^{2+} and $Co^{3+/4+}$.

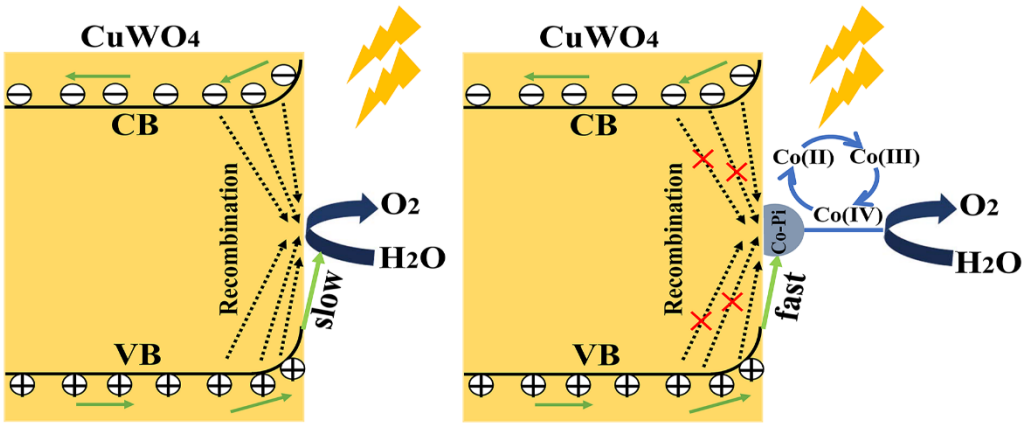

Figure 7. Schematic illustration of the charge-transfer mechanism for Co-Pi-modified $CuWO_4$ during illumination.

4. CONCLUSIONS

In summary, Co-Pi as an efficient cocatalyst was electrodeposited onto $CuWO_4$ NFs *via* a CV method to further enhance the photocatalytic activity of $CuWO_4$ toward PEC OER. After Co-Pi modification, the photocurrent density as well as the charge-transfer efficiency was improved within the entire potential range. Besides, the $CuWO_4$/Co-Pi composite photoanode exhibited an enhanced stability toward PEC OER over the bare $CuWO_4$ in the phosphate buffer solution (pH 7) and a high Faradaic efficiency of *ca.* 96%. Our work demonstrates that the combination of $CuWO_4$ with Co-Pi is an efficient way to promote the performance of $CuWO_4$ for solar water splitting.

ACKNOWLEDGMENTS
We gratefully acknowledge the financial support of this work by National Natural Science Foundation of China (NSFC 51672017, 51872015, and 51604310), Beijing Natural Science Foundation (2142020 and 2151001). Open Foundation of State Key Laboratory of Environmental Protection for Iron and Steel Industry (2016YZC03).

References

1. T. A. Betley, Q. Wu, V. T. Van, and D. G. Nocera, *Inorg Chem.*, 47 (2008) 1849.
2. J. K. Hurst., *Science*, 328 (2010) 315.
3. M. Gratzel, *Nature*, 414 (2001) 338.
4. M. G. Walter, E. L. Warren, J. R. Mckone, S. W. Boettcher, Q. Mi, E. A. Santori, and N. S. Lewis, *Chem Rev.*, 110 (2010) 6446.
5. J. Sun, D. K. Zhong, and D. R. Gamelin, *Energy Environ. Sci.*, 3 (2010) 1252.
6. Q. Wu, P. Diao, J. Sun, D. Xu, T. Jin, and M. Xiang, *J. Mater. Chem. A.*, 3 (2015) 18991.
7. D. Chandra, K. Saito, T. Yui, and M. Yagi, *ACS Sustainable Chem. Eng.*, 6 (2018) 16838.
8. H. S. Han, S. Shin, D. H. Kim, I. J. Park, J. S. Kim, P.-S. Huang, J.-K. Lee, I. S. Cho, and X. Zheng, *Energy Environ. Sci.*, 11 (2018) 1299.
9. Z. Wu, Z. Zhao, G. Cheung, R. M. Doughty, A. R. Ballestas-Barrientos, B. Hirmez, R. Han, T. Maschmeyer, and F. E. Osterloh, *J. Electrochem. Soc.*, 166 (2018) H3014.
10. J. E. Yourey, and B. M. Bartlett, *J. Mater. Chem.*, 21 (2011) 7651.
11. H. Zhang, P. Yilmaz, J. O. Ansari, F. F. Khan, R. Binions, S. Krause, and S. Dunn, *J. Mater. Chem. A.*, 3 (2015) 9638.
12. Y. Gao, O. Zandi, and T. W. Hamann, *J. Mater. Chem. A.*, 4 (2016) 2826.
13. J. Yang, C. Li, and P. Diao, *Electrochim. Acta*, 308 (2019) 195.
14. C. M. Tian, M. Jiang, D. Tang, L. Qiao, H. Y. Xiao, F. E. Oropeza, J. P. Hofmann, E. J. M. Hensen, A. Tadich, W. Li, D. C. Qi, and K. H. L. Zhang, *J. Mater. Chem. A.*, 7 (2019) 11895.
15. B. Peng, C. Li, C. Yue, and P. Diao, *Int. J. Electrochem. Sci.*, 14 (2019) 2574.
16. K. J. Pyper, J. E. Yourey, and B. M. Bartlett, *J. Phys. Chem. C.*, 117 (2013) 24726.
17. J. E. Yourey, K. J. Pyper, J. B. Kurtz, and B. M. Bartlett, *J. Phys. Chem. C.*, 117 (2013) 8708.
18. D. Hu, P. Diao, D. Xu, M. Xia, Y. Gu, Q. Wu, C. Li, and S. Yang, *Nanoscale*, 8 (2016) 5892.
19. W. Ye, F. Chen, F. Zhao, N. Han, and Y. Li, *ACS Appl. Mater. Interfaces.*, 8 (2016) 9211.
20. Y. Tang, N. Rong, F. Liu, M. Chu, H. Dong, Y. Zhang, and P. Xiao, *Appl. Surf. Sci.*, 361 (2016) 133.
21. J. C. Hill, and K.-S. Choi, *J. Mater. Chem. A.*, 1 (2013) 5006.
22. N. Gaillard, Y. Chang, A. DeAngelis, S. Higgins, and A. Braun, *Int. J. Hydrogen Energy*, 38 (2013) 3166.
23. M. Valenti, D. Dolat, G. Biskos, A. Schmidt-Ott, and W. A. Smith, *J. Phys. Chem. C.*, 119 (2015)

2096.
24. A. E. B. Lima, M. J. S. Costa, R. S. Santos, N. C. Batista, L. S. Cavalcante, E. Longo, and G. E. Luz, *Electrochim. Acta*, 256 (2017) 139.
25. M. Davi, A. Drichel, M. Mann, T. Scholz, F. Schrader, A. Rokicinska, P. Kustrowski, R. Dronskowski, and A. Slabon, *J. Phys. Chem. C.*, 121 (2017) 26265.
26. D. Peeters, O. Mendoza Reyes, L. Mai, A. Sadlo, S. Cwik, D. Rogalla, H. W. Becker, H. M. Schütz, J. Hirst, S. Müller, D. Friedrich, D. Mitoraj, M. Nagli, M. C. Toroker, R. Eichberger, R. Beranek, and A. Devi, *J. Mater. Chem. A.*, 6 (2018) 10206.
27. S. S. Kalanur, J.-Y. Hwang, and H. Seo, *J. Catal.*, 350 (2017) 197.
28. R. Liu, Y. Lin, L. Y. Chou, S. W. Sheehan, W. He, F. Zhang, H. J. Hou, and D. Wang, *Angew. Chem., Int. Ed. Engl.*, 50 (2011) 499.
29. S. D. Tilley, M. Cornuz, K. Sivula, and M. Gratzel, *Angew. Chem., Int. Ed. Engl.*, 49 (2010) 6405.
30. H. Yoo, K. Oh, G. Lee, and J. Choi, *J. Electrochem. Soc.*, 164 (2017) H104.
31. Y. Fan and X. Cheng, *J. Electrochem. Soc.*, 163 (2016) E209.
32. M. W. Kanan and D. G. Nocera, *Science*, 321 (2008) 1072.
33. M. Dinca, Y. Surendranath, and D. G. Nocera, *Proc. Natl. Acad. Sci. U. S. A.*, 107 (2010) 10337.
34. T. W. Kim and K. S. Choi, *Science*, 45 (2014) 990.
35. E. M. Steinmiller and K. S. Choi, *Proc. Natl. Acad. Sci. U. S. A.*, 106 (2009) 20633.
36. C. Ma, Z. Liu, Q. Cai, C. Han, and Z. Tong, *Inorg. Chem. Front*, 5 (2018) 2571.
37. J. A. Seabold and K.-S. Choi, *Chem. Mater.*, 23 (2011) 1105.
38. D. K. Zhong, J. Sun, H. Inumaru, and D. R. Gamelin, *J. Am. Chem. Soc.*, 131 (2009) 6086.
39. D. K. Zhong and D. R. Gamelin, *J. Am. Chem. Soc.*, 132 (2010) 4202.
40. D. K. Zhong, M. Cornuz, K. Sivula, M. Grätzel and D. R. Gamelin, *Energ. Environ. Sci.*, 4 (2011) 1795.
41. X. Shi, K. Zhang, and J. H. Park, *Int. J. Hydrogen Energy*, 38 (2013) 12725.
42. T. H. Jeon, W. Choi, and H. Park, *Phys. Chem. Chem. Phys.*, 13 (2011) 21392.
43. F. F. Abdi and R. van de Krol, *J. Phys. Chem. C.*, 116 (2012) 9398.
44. R. Tong, X. Wang, X. Zhou, Q. Liu, H. Wang, X. Peng, X. Liu, Z. Zhang, H. Wang, and P. D. Lund, *Int. J. Hydrogen Energy*, 42 (2017) 5496.
45. M. Davi, M. Mann, Z. Ma, F. Schrader, A. Drichel, S. Budnyk, A. Rokicinska, P. Kustrowski, R. Dronskowski, and A. Slabon, *Langmuir*, 34 (2018) 3845.
46. C. R. Lhermitte and B. M. Bartlett, *Acc. Chem. Res.*, 49 (2016) 1121.
47. K. M. Nam, E. A. Cheon, W. J. Shin, and A. J. Bard, *Langmuir*, 31 (2015) 10897.
48. S. Chen, M. N. Hossain, and A. Chen, *ChemElectroChem.*, 5 (2018) 523.
49. M. Zhou, Z. Liu, Q. Song, X. Li, B. Chen, and Z. Liu, *Appl. Catal. B.*, 244 (2019) 188.
50. Y. Surendranath, M. W. Kanan, and D. G. Nocera, *J. Am. Chem. Soc.*, 132 (2010) 16501.
51. J. G. Mcalpin, Y. Surendranath, M. Dincă, T. A. Stich, S. A. Stoian, W. H. Casey, D. G. Nocera, and R. D. Britt, *J. Am. Chem. Soc.*, 132 (2010) 6882.
52. Y. Gao and T. W. Hamann, *Chem. Commun.*, 53 (2017) 1285.
53. Y. Gao and T. W. Hamann, *J. Phys. Chem. Lett.*, 8 (2017) 2700.
54. D. A. Lutterman, Y. Surendranath, and D. G. Nocera, *J. Am. Chem. Soc.*, 131 (2009) 3838.
55. D. Hu, P. Diao, D. Xu, and Q. Wu, *Nano Res.*, 9 (2016) 1735.